Review article

Performance benchmarking and analysis of lithium-sulfur batteries for next-generation cell design

Saeed Yari[1,2,3], Albin Conde Reis[1,2], Quanquan Pang ◑[4] & Mohammadhosein Safari ◑[1,2,3] ✉

Lithium-sulfur batteries are emerging as strong contenders in energy storage; however, a cohesive design framework, systematic performance analysis and benchmarks remain absent. This study bridges this gap by examining recent advancements, with a focus on functional sulfur host materials, using a data-driven approach. Through a meticulous literature review, we digitize 866 galvanostatic cycling and rate capability plots, along with the collection of key host material properties—such as specific surface area and polysulfide binding/adsorption energy—as well as essential cell design parameters including sulfur loading, electrode formulation, and electrolyte-to-sulfur ratios, to standardize performance using specific energy and power metrics. This approach enables us mapping field advancements and identify impactful research contributions. Additionally, irrespective of materials chemistry, a comprehensive analysis of this database helps us to disclose general patterns that apply universally across all cells, highlight the most constructive and detrimental regions of the design-parameter space, and perceive potential synergies. These insights outline key areas for optimization, guiding future development of practical lithium-sulfur battery technology.

Lithium-sulfur batteries (LSBs) are rapidly establishing themselves as formidable competitors in the energy storage sector, offering an impressive theoretical specific energy of 2600 Wh/kg, with the prospect of reaching a practical cell-level specific energy of 500 Wh/kg[1]. The appeal of LSBs is further amplified by the abundance of raw materials, cost-effectiveness, and reduced environmental impact[2]. A typical LSB cell is constructed with a lithium metal anode, an organic liquid electrolyte, and a composite sulfur (S_8) cathode. During the discharge of a LSB with a conventional ether-based electrolytes, sulfur reduces to the final discharge products, lithium sulfide (Li_2S_2/Li_2S), in two distinct stages (Fig. S1)[3]:

Stage 1: S_8 (solid) → Li_2S_6 (liquid) → Li_2S_4 (liquid) **Stage 2:** Li_2S_4 (liquid) → Li_2S_2/Li_2S (solid).

This sequential transformation highlights the complex redox processes that govern LSB performance, and cause practical LSB solutions to face some major challenges, including: (1) low electronic conductivity in sulfur and Li_2S limits performance; (2) polysulfide solubility in electrolytes causes sulfur loss, self-discharge, and the shuttle effect; (3) volume changes during $S \rightleftharpoons Li_2S$ conversions lead to structural issues; and (4) the lithium anode struggles with unstable solid electrolyte interphase and dendrite formation[4–6].

Extensive research has been dedicated to unlocking the full potential of LSB technology, addressing its issues in various ways. Our preliminary survey of 842 recent research articles on LSBs shows that the largest portion of these scholarly works (38.6%) aim to tackle these challenges by development of a functional sulfur host (Fig S2), offering features such as high electronic and ionic conductivity, porous

[1]Institute for Materials Research (IMO-imomec), UHasselt, Martelarenlaan 42, 3500 Hasselt, Belgium. [2]Energyville, Thor Park 8320, 3600 Genk, Belgium. [3]IMEC Division IMOMEC, 3590 Diepenbeek, Belgium. [4]Beijing Key Laboratory for Theory and Technology of Advanced Battery Materials, School of Materials Science and Engineering, Peking University, 100871 Beijing, China. ✉e-mail: momo.safari@uhasselt.be

structure, large surface area, or providing active sites within this framework that serve as polysulfide adsorbers, immobilizers, or redox mediators[5]. The incorporation of sulfur into this structure produces a novel active material. This material is subsequently mixed with a conductive additive, such as carbon black or acetylene black, along with a binder. The resulting mixture is dispersed in a solvent to form a slurry, which is then coated on a current collector to fabricate an electrode, similar to the process used in Li-ion battery electrode production.

This study aims to benchmark and analyze LSB performance, focusing on the literature with functional sulfur hosts, as the main contributor to advance this technology. We calculate cell-level specific energy (Wh/kg) and specific power (W/kg) to establish a framework for evaluating advancements and guiding LSB design toward improved energy, power, and cycle life. Key host material properties such as specific surface area and polysulfide binding/adsorption energy and essential cell design parameters required for these calculations—including electrolyte-to-sulfur ratio (E/S), sulfur loading, sulfur weight percentage, and reversible capacity per gram of sulfur—were extracted from the literature. Performance metrics were gathered through plot digitization, yielding a substantial dataset from 866 plots (670 cycling performance and 196 rate capability plots) from 184 recent articles. We believe this approach offers valuable insights and contributes to organizing and standardizing the scattered data in the literature. Additionally, we conducted a comprehensive analysis to systematically evaluate how individual parameters influence performance metrics. Our primary focus was on univariate analysis, where we isolated each parameter to uncover clear and consistent trends without interference from overlapping variables. This approach serves as a strong foundation for identifying distinct patterns with high clarity.

LSB performance benchmarking and analysis
Benchmarking cell specific energy
The general structure of an LSB cell with a liquid electrolyte and a cathode formulated with a functional sulfur host is schematized in Fig. 1a. By determining the weight of each component, the cell-level specific energy (Wh/kg), excluding the packaging weight, can be readily calculated using Eq. 1:

$$E_s = \frac{M.Q^s_{rev}.V}{M.\gamma.\rho_{El} + \frac{M}{f_s^s} + \frac{\delta.M.Q^s_{rev}}{Q^{Li}_{rev}} + \frac{\rho_{sep}.t_{sep}}{10} + \frac{\rho_{Al}.t_{Al}}{10} + \frac{\rho_{Cu}.t_{Cu}}{10}}$$

(1)

Specific power (W/kg) is C-rate dependent. It can be calculated using a slightly modified version of Eq. 1 and using C-rate (C), measured in units of 1/h, as an extra input:

$$P_s = \frac{M.Q^s_R.V_R.C}{M.\gamma.\rho_{El} + \frac{M}{f_s^s} + \frac{\delta.M.Q^s_{rev}}{Q^{Li}_{rev}} + \frac{\rho_{sep}.t_{sep}}{10} + \frac{\rho_{Al}.t_{Al}}{10} + \frac{\rho_{Cu}.t_{Cu}}{10}}$$

(2)

where Q^s_R and V_R represents the discharge capacity and average discharge voltage at a specific C-rate, respectively. Table 1 provides a detailed description of the variables used to calculate E_s and P_s. We assumed V_R (in Eq. 2) exhibits negligible sensitivity to the C-rate, as well as to specific electrode and electrolyte parameters, and approximated it as equal to the cell's nominal voltage. This assumption was adopted because discharge voltage values at different C-rates are most often unavailable in the literature. However, we acknowledge that at higher C-rates, polarization influences the discharge voltage. The thicknesses of the Al and Cu current collectors, as well as the separator,

are assumed to be among the thinnest available, even though studies often use relatively thicker materials, such as Celgard 2400 separator. The key consideration is that a practical cell is designed to incorporate the most advanced and lightweight components available (e.g., Monolayer Celgard PP1410 with a thickness of 14 μm), rather than those commonly used in past studies.

As a standard practice in battery design, we assume the anode capacity to be larger than the cathode capacity, defined by the negative-to-positive (N/P) ratio. This approach enhances stability and mitigates the risk of catastrophic failure by compensating for minor losses of anode active material. In commercial Li-ion batteries with graphite anodes, a 10–20% excess anode is typically used to prevent Li plating and accelerated side reactions, which corresponds to N/P ratio of 1.1–1.2[7]. In our analysis, we assume an N/P ratio of 1.5—higher than that of Li-ion cells due to the more severe degradation of lithium anodes, but not excessively high to the point of negating energy density gains in Li-metal batteries. As highlighted in the study by Nanda and Manthiram[8], the loss of lithium inventory is a predominant degradation mechanism in LSBs. In controlled laboratory settings, lithium metal foils with thicknesses ranging from 200 to 400 μm, i.e., significantly higher N/P ratios, are typically employed for cell assembly which can compensate for the accelerated loss of lithium. However, in our study, we have deliberately chosen an N/P ratio of 1.5 to provide a standardized and realistic benchmarking framework across different cells. This approach ensures a more pragmatic assessment of performance, particularly when considering future advancements—such as optimized electrolyte formulations and engineered solid electrolyte interphases (SEI)—[9] in lithium metal battery technology. Without these innovations, the long-term viability of such batteries would remain in question.

Figure 1b, c illustrate the sensitivity of an LSB cells' specific energy to reversible discharge capacity, sulfur loading and E/S ratio, based on Eq. 1, for sulfur contents of 56 wt.% and 80 wt.% (representing median and maximum values, see Fig. S3) and sulfur loadings up to 20 mg/cm² (the identified maximum, see Fig. S3). Though in an ideal situation, decreasing the E/S ratio or increasing sulfur loading or sulfur wt.% can unconditionally raise the cell specific energy, it does not necessarily happen in practice. In Fig. 1d, we illustrate the reversible discharge capacity values, Q^s_{rev}, for the cells with different sulfur loadings and E/S ratios. The electrolyte in majority of cells consisted of 1 M lithium bis(trifluoromethanesulfonyl)imide (LiTFSI) in 1:1 (V:V) 1,3-Dioxolane and Dimethoxyethane (DOL:DME) with ~0.5–2 wt.% of LiNO₃ (see Table S1). At low sulfur loadings and high E/S ratios, high Q^s_{rev} values are achievable. However, as sulfur loading increases and the E/S ratio decreases, electronic and ionic transport limitations intensify on account of the side effects involved with thicker electrodes, i.e., larger inhomogeneities[10], and lean electrolyte conditions. This can notably reduce the discharge capacity, even at 0.1 C, to as low as 300–400 mAh/g. As shown in

Figure S3, approximately 2 mg/cm² of sulfur is sufficient to reach an areal capacity of 2.5 mAh/cm² (that falls within relatively *thin electrode* range). In contrast, to achieve 10 mAh/cm², around 11.5 mg/cm² of sulfur is needed, which does not result in a proportionate increase in areal capacity. This deviation of projected capacity from that suggested by the thinner electrode design becomes more pronounced at sulfur loadings above ~6 mg/cm², or 7.5 mAh/cm² (Fig. S4). Indeed, any benefits from *excessive* sulfur loading or reduced electrolyte volume can be compromised by the severe cell polarization, and reduction in reversible capacity, pointing at the existence of an optimal level. In addition, according to the pairwise relationships in Fig. 1e, the correlation between E/S and specific energy is notably stronger ($r = -0.8$), than that between sulfur loading and specific energy ($r = +0.50$). Furthermore, despite the modest strength of the correlations between E/S or sulfur loading and capacity retention, the correlation with sulfur loading ($r = -0.28$) is still stronger (which is not good) than that with
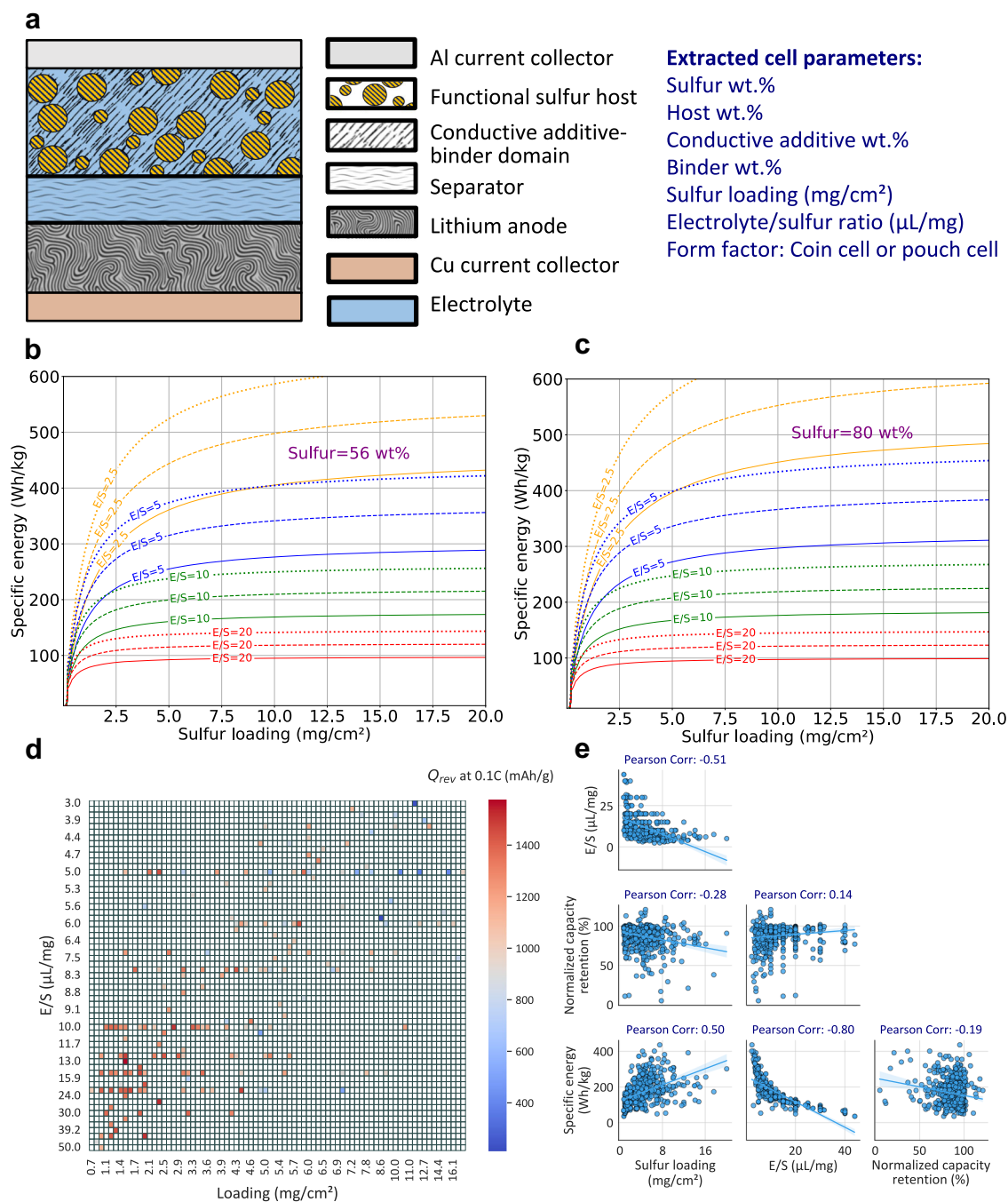
Fig. 1 | LSB cell structure and performance sensitivity to design parameters.
a The structure of a typical LSB cell with a functional sulfur host at the cathode together with an associated list of critical design parameters. **b** Sensitivity of an LSB cells' specific energy to reversible discharge capacity, sulfur loading, and E/S ratio, as calculated using Eq. 1, for sulfur content of 56 wt% and **c** sulfur content of 80 wt%. Dotted line, dashed line, and solid line indicate reversible discharge capacity (Q_{rev}^s) of 1000, 1250, and 1500 mAh/g, respectively. **d** Heatmap of discharge capacity at 0.1 C (representing Q_{rev}^s) as a function of sulfur loading and the E/S ratio. **e** Pairwise correlations between sulfur loading, electrolyte-to-sulfur (E/S) ratio, specific energy, and normalized capacity retention (see Methods). Source data are provided as a Source Data file.

E/S ($r = 0.14$). These observations carry significant implications; decreasing the E/S ratio not only significantly boosts the specific energy but also entails a smaller penalty to the cycling stability, whereas increasing sulfur loading has a more detrimental effect on the capacity retention. This finding highlights the practical significance of prioritizing E/S ratios over sulfur loading for optimizing LSB performance.

Figure 2a presents a map depicting the calculated specific energy and capacity retention for all battery cells in our dataset. In the absence

of explicit temperature data, which was most often the case, we assumed that measurements were conducted under standard ambient laboratory conditions (~25 °C). Cells reported to operate at temperatures significantly above or below ambient were excluded from the dataset when such deviations were specified. According to Eq. 1, cells with thinner electrodes and higher E/S ratios exhibit lower specific energy values. As shown, there is a high concentration of low-energy cells in the 100 to 150 Wh/kg range. Notably, two distinct types of battery cells have frequently been used to demonstrate the

Table 1 | Description of the variables used in Eqs. 1 & 2 to calculate E_s and P_s

Variable (unit)	Description	Value/Source
M (mg/cm²)	Sulfur loading in the cathode	Extracted
Q^s_{rev} (mAh/g)	Reversible/nominal capacity per gram of sulfur	Extracted, equivalent to first cycle discharge capacity at 0.1 C (see Methods)
V (V)	Cell discharge average/nominal voltage	Barely reported, assumed 2.15 V
γ (µl/mg)	Electrolyte-to-sulfur ratio (i.e., E/S)	Extracted
ρ_{el} (g/cm³)	Electrolyte density	Approximately 1 g/cm³ for DOL:DME, V:V 1:1, 1M LiTFSi
f^c_s	Fraction of sulfur in the cathode	Calculated, based on the extracted values of sulfur wt.%, host wt.%, conductive additive wt.%, and binder wt.%
δ	Negative-to-positive capacity ratio	Assumed 1.5
Q^{Li}_{rev} (mAh/g)	Lithium specific capacity	3860 mAh/g
t_{sep} (µm)	Separator thickness	Assumed 14 µm
ρ_{sep} (g/cm³)	Separator density	0.46 g/cm³ (for a microporous PP membrane with 50% porosity)
t_{al} (µm)	Aluminum thickness	Assumed 5 µm (10 µm current collector for double sided coating), 0 for freestanding electrodes
ρ_{Al} (g/cm³)	Aluminum density	2.7 g/cm³
t_{cu} (µm)	Copper thickness	Assumed 5 µm (10 µm current collector for double sided coating)
ρ_{cu} (g/cm³)	Copper density	8.96 g/cm³

functionality of new sulfur hosts. The first type, referred to as "standard cells," typically features thin electrodes with low sulfur loading and a high E/S ratio. This configuration minimizes cell polarization and serves as a proof-of-concept to validate new materials. The second type, known as "practical cells," includes electrodes with higher sulfur loadings, reduced electrolyte volumes, or both. These cells are designed to assess the feasibility of new materials in high-energy-density applications that are closer to real-world use.

Cycling at higher discharge C-rates has been predominantly performed with standard cells. As evident in the data, above 200 Wh/kg, very few cells have been cycled at rates exceeding 1 C. This suggests that cells with thicker electrodes and lower E/S ratios are more prone to failure under high C-rate conditions. However, an interesting observation is that the capacity retention of cells cycled at high C-rates is largely concentrated above 90%–a point of interest that will be explored further in this article. Pouch cell batteries, typically constructed with thicker electrodes and lower E/S ratios, generally show lower capacity retention than most coin cells. Notably, most of these pouch cells have been cycled at relatively low rates (0.1–0.2 C).

Additionally, it should be noted that unlike thick-electrode cells under lean electrolyte conditions, which are prone to early catastrophic failure, potentially occurring after just a few tens of cycles, thin-electrode cells with high electrolyte volumes demonstrate extended cycling beyond the 100-cycle threshold used for capacity retention normalization (See Methods). However, catastrophic failure was almost never observed in our dataset, and significant variations in lifecycle assessment measurements (e.g., different final cycle counts) were present. To ensure a consistent benchmarking framework, we relied on normalized capacity retention as a standard comparative metric across all cells. This approach assumes that catastrophic failure is not imminent, allowing us to track degradation through the entire cycle life without reaching a failure point, and ensuring a consistent basis for comparison. It would have also been valuable to include Coulombic efficiency (CE) in our analysis, as even small variations (e.g., 99.5% vs. 99.9%) can serve as key indicators of lithium loss, electrolyte degradation, and side reactions–factors that accumulate over cycles and impact long-term performance. However, CE is typically plotted over cycles with values very close to 100%, making it difficult to extract meaningful data using our method. Our approach, designed to capture overall trends rather than subtle fluctuations, lacks the precise digitization required for an accurate CE analysis.

In Fig. 2b, we focused on cells identified with sulfur loadings above 4 mg/cm² and E/S ratios below 5 µl/mg[11–49]. The most energy-dense cell

achieved an impressive 441 Wh/kg (with an estimated volumetric energy density of 555 Wh/L, See Table S3) with lithiated MoS₂ as the host material, sulfur loading of 7.5 mg/cm² and E/S equal to 2.4 µl/mg, demonstrating stable cyclability at ~0.5 C in pouch cell format. A noteworthy observation from Fig. 2b is the small specific energy of some battery cells, which can be as low as 100 Wh/kg. According to Table 2, exceptionally high sulfur loadings (11.6 mg/cm² and 14.8 mg/cm²) lead to a significant decrease in reversible discharge capacity, negating any energy benefits from lean electrolyte condition and resulting in low specific energy values. Nevertheless, the median specific energy for all these cells is 298 Wh/kg. This suggests that the functional sulfur hosts are performing exceptionally well, and despite the potential for further improvements in sulfur loading and E/S ratios, these cells already outperform commercial Li-ion cells in terms of specific energy. Our findings are based mainly on coin cells, which, while useful for testing and prototyping, have limitations like uneven electrolyte distribution affecting electrode contact. However, a rough estimates of current performance trends and positioning different research efforts in relation to one another was achievable.

Further advancements in material technology could push LSB cell specific energy beyond 500 Wh/kg. Sulfur-impregnated lithiated MoS₂ (64:36 sulfur-to-host ratio) innovated by Li et al.[11] has demonstrated a discharge capacity of ~1423 mAh/g at 0.1 C under standard conditions (12 µl/mg E/S ratio, 2.5 mg/cm² of sulfur loading). However, there is still room for improvement in both reversible discharge capacity and sulfur-to-host ratio for further gain in specific energy–though a major breakthrough in material innovation is indeed required. Achieving electrode loadings beyond 7.5 mg/cm², presents challenges, but advanced techniques such as dry coating[50], optimized slurry formulation, and active material particle size regulation may enable higher loadings[51]. A key limitation remains the E/S ratio: even in the most energy-dense cell, the electrolyte still constitutes nearly 46% of the total mass (See Table S3 and Fig. S5). In the DOL:DME 1 M LiTFSI electrolyte system, studies indicate that Li₂S deposition ceases below an E/S ratio of 2.4 µl/mg[52], which was also the threshold identified by Li et al.[11] Therefore, further reduction in electrolyte volume needs the exploration of alternative strategies.

One potential approach to further reduce the E/S ratio is to move beyond the conventional moderately solvating electrolyte (MSE) system, such as DOL:DME/LiTFSI, and explore alternative electrolyte designs. Two promising classes have attracted significant interest: sparingly solvating electrolytes (SSEs)–including high-concentration electrolytes and hydrofluoroether-based systems–and highly
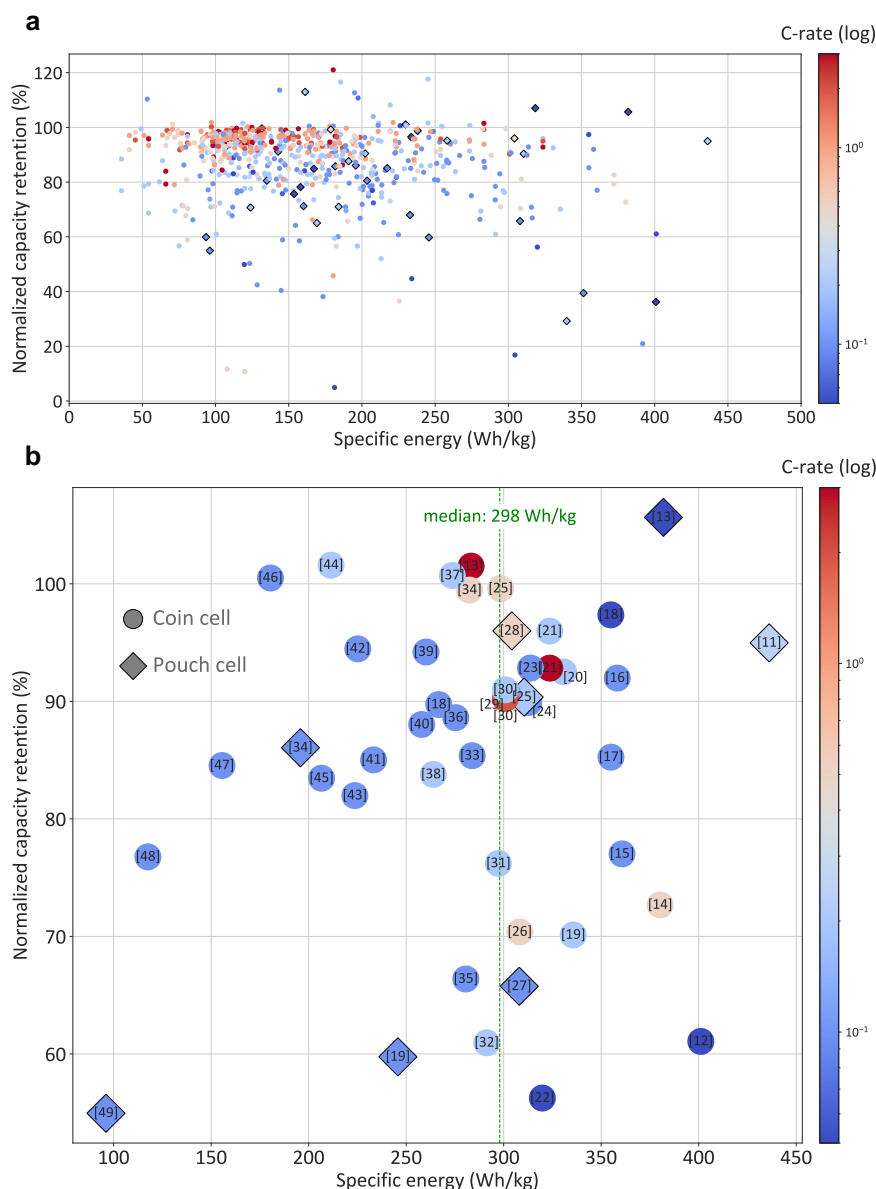
Fig. 2 | Benchmarking specific energy and capacity retention across LSB designs. Calculated specific energy and capacity retention for **a** all the battery cells identified in our literature survey **b** for cells with E/S ratios below or equal to 5 μl/mg and sulfur loadings above and equal to 4 mg/cm², and normalized capacity retention of above 50% (see Table S2 for design and performance details). Often, there was a gain in capacity beyond the values at initial cycle suggesting the gradual activation of active materials over time, likely due to sulfur redistribution. Source data are provided as a Source Data file.

solvating electrolytes (HSEs), which typically consist of solvents with a high donor number (DN) or high permittivity (ε)[53]. SSEs possess unique solvation properties that limit excessive solvent interactions with lithium polysulfides, thereby reducing the E/S ratio required for sulfur reduction. In contrast, HSEs enhance polysulfide solubility, minimizing electrolyte volume requirements and thus also lowering E/S. These two approaches appear to be opposite sides of the same coin, and share the common advantage of enabling lower E/S ratios—an essential factor for improving the energy density of Li-S batteries.

In addition to the E/S ratio, electrolyte can significantly influence reaction pathway and voltage profiles (see SI for reaction mechanisms). SSEs can increase, maintain, or reduce the average cell voltage; For instance, in hydrofluoroether (HFE)-based electrolyte solutions, two voltage plateaus, similar to those in MSEs, are typically observed[54]. However, the initial plateau occurs at a lower discharge voltage, and as the HFE content increases, the voltage profile declines further, promoting a solid-solid reaction[55]. In high-

concentration electrolytes such as acetonitrile (ACN)₂-LiTFSI/HFE, a slightly higher voltage plateau is observed[56], while, an equipotential bi-plateau voltage profile with a quasi-solid-solid reaction can be seen in systems like diethylene glycol dimethyl ether (G2):LiTFSI[57]. On the other hand, in HSEs with high-DN solvents generally the first discharge plateau elevates, owing to the lower solvation energy of Li^+ ions in high-DN solvents of HSEs[58], which consequently, increases the energy density as described by Eq. I.

Another critical factor in electrolyte selection is density, which must be carefully managed to optimize cell performance. While alternative electrolytes can help reduce the E/S ratio, their density plays a crucial role. For instance, high-concentration electrolyte systems can reach densities of up to ~1.6 g/cm³[53]. In Fig. S6, we plotted the sensitivity of the specific energy of a typical LSB to a hypothetic simultaneous decrease in the E/S ratio from 2.5 μl/mg to 1 μl/mg and an increase in electrolyte density from 1 to 1.6 g/cm³. Although a net gain in specific energy is observed, the increased electrolyte density

Table 2 | Design parameters for the top 5 percentile LSB cells with the highest and lowest specific energy among cells with E/S ratios below 5 μl/mg and sulfur loadings above 4 mg/cm²

References	Q_{rev} at 0.1C (mAh/g)	Specific energy, E_s (Wh/kg)	Normalized capacity retention (%)	Sulfur loading (mg/cm²)	E/S (μl/mg)	S/Functional host ratio (mg/mg)	Conductive additive (wt.%)	Category
11	1061.3	436.1[a]	95	7.5	2.4	2.5	0	High E_s
12	1040.2	401.1	61.1	6.5	2.3	1.5	10	High E_s
13	1022.3	381.9	105.7	8.4	3	2.3	0	High E_s
47	554	155.6	84.5	7.4	5	4	10	Low E_s
48	403.6	117.6	76.8	14.8	5	4	20	Low E_s
49	225	96.1	55	11.6	3	9	10	Low E_s

[a]441 Wh/kg as precisely reported by the innovators.

introduces a trade-off by adding to the cell mass. Therefore, achieving meaningful energy density improvements requires a balanced approach that optimizes both the E/S ratio (i.e., volume) and electrolyte mass.

Here, a discussion of LSB cells with Li₂S cathodes is also worthwhile. Even though they operate on the same principles as elemental sulfur cathodes, the different state of the initial cathode allows for interesting opportunities. For instance, Li₂S cathodes are often combined with solid electrolytes[59,60], or, as they can also be the source of lithium, they allow the use of Li-free anodes such as graphite which increases the cell safety[61,62]. A performance comparison of LSB cells with Li₂S cathodes is presented in Fig. S7. However, variations in cell design due to differences in electrolyte and anode selection, along with the inconsistent reporting of E/S ratio and loading, significantly reduced the size of our dataset. Moreover, since the anode is lithium metal in our benchmarking framework, the analysis does not accurately reflect the energy density of practical Li₂S cells but rather represents a "half-cell" Li₂S system using a metallic lithium anode.

Based on this small dataset, we did not find any Li₂S-based cell exceeding the highest specific energy observed in Fig. 2b. However, Li₂S appears to offer a slight advantage in capacity retention, with most cells falling within the 80–100% capacity retention, but, due to the limited number of observations, a definitive conclusion cannot be drawn. We see Li₂S as a niche alternative to S₈, offering unique opportunities for cell design and optimization. No dominant configuration (anode, electrolyte) has yet emerged, and few studies explore practical conditions such as high loadings, low passive material ratios, or high C-rates. While Li₂S-based cell has yet to match the energy density of S₈-based LSBs, it may provide other benefits, including better compatibility with solid electrolytes, longer lifespan, and improved safety. To establish a stronger basis for comparison in future research, we strongly encourage authors to report key parameters (N/P ratio, E/S ratio, loadings) and provide energy density estimates at the cell level.

Design innovations in sulfur host materials. The design of sulfur host materials fundamentally revolves around optimizing two critical structural and functional attributes. First, the architectural framework must enable efficient polysulfide confinement and Li₂S precipitation through carefully engineered pore distribution, enhanced electrolyte accessibility, and the regulation of surface area. Second, the host must enhance electrochemical performance through polysulfide adsorption and catalytic activity, which accelerate redox kinetics, promote reversible sulfur conversion, and mitigate polysulfide shuttling[63]. In our database, we could roughly classify sulfur host architectures into the following categories (Fig. 3a): (i) porous carbon structures, (ii) metal-organic framework (MOF)-derived porous particles; (iii) templated ordered structures; (iv) hollow structures, such as nanotubes, nanospheres, and hollow cubes; (v) zero-dimensional (0D) non-porous

particles; (vi) one-dimensional (1D) nanostructures, including nanotubes and nanorods; (vii) two-dimensional (2D) hosts, such as MXenes, nanosheets, graphene-like materials, their assembled flower-like architectures, which maximize active surface exposure and electronic conductivity, or 2D materials grown on 1D substrates, where the primary structural unit remains 2D but is supported by a 1D scaffold; and (viii) hierarchical three-dimensional (3D) assemblies, which integrate 1D and 2D building blocks into complex, interconnected frameworks.

Among the structural features of sulfur host materials, the Brunauer-Emmett-Teller (BET) surface area is the most commonly reported and accessible parameter. Porous carbon materials show the highest surface area (Fig. 3b). A few hollow structures also rank among the highest surface areas, while most other materials fall within the 100–400 m²/g range. Figure 3c illustrates the relationship between surface area and reversible capacity in standard cells (with sufficient electrolyte and thin electrodes). Both the highest and lowest reversible discharge capacities are typically observed in materials with surface areas below 500 m²/g, with optimal performance occurring around 400 m²/g. Notably, when the surface area exceeds 500 m²/g, discharge capacities rarely surpass ~1400 mAh/g. Ironically, despite their high surface areas, porous carbon hosts demonstrate the poorest performance in our database (Fig. S8).

The required surface area for a given host materials can be approximated considering that a full discharge of 1 mole of S₈ with a molar mass of 256.56 g/mole results in the production of 8 moles of Li₂S with a molar mass of 45.95 g/mole and density of 1.66 g/cm³. Therefore, neglecting the 3D growth, we can estimate the surface area A (m²/g) required for a particular sulfur-to-host weight ratio p (grams of sulfur per gram of host) and Li₂S thickness t (in nm):

$$A = \frac{8 M_{Li_2S}}{M_{S_8}} \times \frac{1}{\rho_{Li_2S}} \times \frac{1}{t_{Li_2S} \times 10^{-7}} \times p \qquad (3)$$

$$A = \frac{863}{t} \times p \, (\text{m}^2/\text{g of host}) \qquad (4)$$

In Fig. S9, we present a plot of the required surface area as a function of both sulfur-to-host ratio and Li₂S thickness, t. According to Klein et al.[64], at a low C-rate of C/12, Li₂S films as thick as 30 nm can be charged without encountering significant overpotentials. However, as the C-rate increases, the permissible thickness of the Li₂S layer decreases. Based on our data (Fig. S9), for a sulfur-to-host ratio of 3, the required surface area for Li₂S thicknesses between 5 and 30 nm ranges from 100 to 500 m²/g. Notably, this range closely aligns with the surface areas at which we observed the highest discharge capacities in our dataset. Indeed, this challenges the common assumption that very high surface areas always benefit LSB performance, at least based on three rationales. Firstly, very high surface area is often associated with
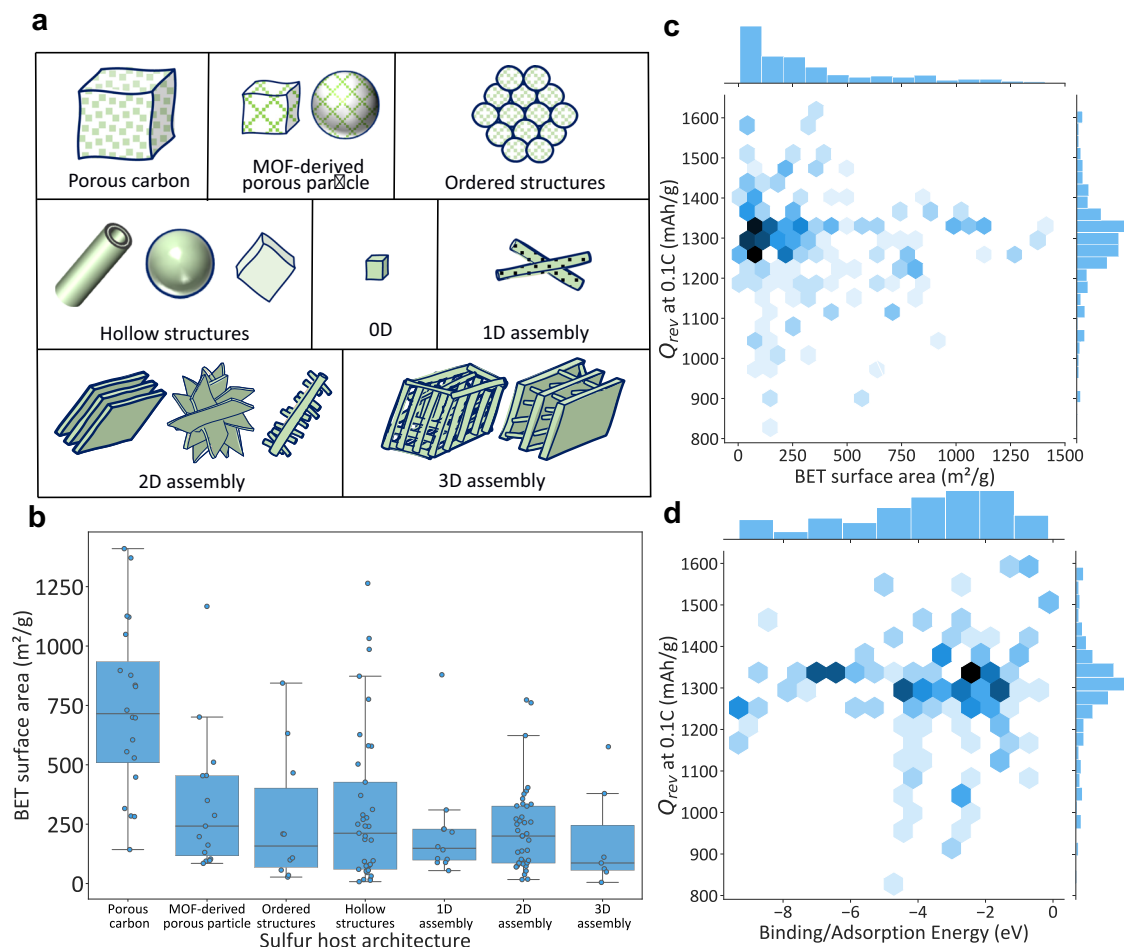
Fig. 3 | Sulfur host architectures, surface area, and performance trends.
a Schematic representation of the different sulfur host architectures categorized in our database. **b** BET surface area distribution across these architectures. The box represents the interquartile range (IQR) from Q1 to Q3, with the center line indicating the median. Whiskers extend to the most extreme data points within [Q1 − 1.5×IQR, Q3 + 1.5×IQR], and outliers beyond this range are shown as individual points. Box median and sample size, n, are provided in Table S4. **c** Reversible discharge capacity of cells with hosts of varying specific surface areas. **d** Reversible discharge capacity of cells with hosts exhibiting different Li_2S_6 binding/adsorption energies. Hexagon color intensity encodes point count, with darker bins indicating regions of higher data density. Data is limited to standard cells with sufficient electrolyte and thin electrodes. Source data are provided as a Source Data file.

small pores and highly intricate, tortuous structures, as seen in porous carbon, which can impede effective lithium ion movement. Secondly, it can restrict access and limit sulfur infiltration into hard-to-reach regions or volumes with excessively small pore sizes. Thirdly, excessive surface area can exacerbate electrolyte uptake and promote side reaction[65,66]. This can also partially explain why 2D and hollow structures often achieve higher discharge capacities. These materials not only provide above-average surface areas but also feature spacious voids—either within the hollow core or between building blocks in 2D assemblies—facilitating sulfur impregnation and lithium diffusion.

In many cases, the host structures incorporated functional species such as metals, metal oxides, metal selenides, metal sulfides, metal carbides, metal nitrides, and metal phosphides (See Fig. S10) to enhance polysulfide adsorption and catalytic activity. One notable feature reported in nearly half of our dataset was the adsorption or binding energy calculation of polysulfide species—most commonly Li_2S_6—on the functional host surface. In many studies, polysulfide adsorption was assessed qualitatively through color changes in polysulfide solutions or UV-Vis spectroscopy, which, while indicative, lacked quantifiable data. However, in cases where adsorption energies were explicitly reported, computational methods were typically used for their determination, explaining why only nearly half of our dataset includes this metric. Figure 3d demonstrates the relationship between

reversible discharge capacity and polysulfide binding energy. Interestingly, extremely high binding energies, that are often achieved in metal nitrides (Fig. S10a), did not correspond to the highest capacities. Instead, optimal performance was observed in the low-to-medium binding energy range, suggesting that excessive adsorption can lead to polysulfide immobilization and hinder performance. This univariate analysis doesn't account for other host properties like surface area or catalytic effects. However, the findings highlight the need to better contextualize binding energy within a broader framework that includes surface area and other synergistic factors. Due to incomplete data, a reliable correlation remains elusive, but this is a critical area for future research.

In host material design, other properties such as electronic conductivity, lithium-ion diffusion coefficient, and catalytic activity are also key to performance. However, compiling a reliable database for these parameters proved challenging for several reasons. First, it is widely accepted that higher values generally enhance performance, making their independent evaluation less prioritized. More importantly, inconsistencies in measurement methodologies present a major obstacle. For instance, polysulfide conversion kinetics are assessed through various techniques—such as cyclic voltammetry (CV) peak separation, the relationship between peak current and the square root of scan rate (I vs. $v^{0.5}$), and charge transfer resistance (R_{ct}) from
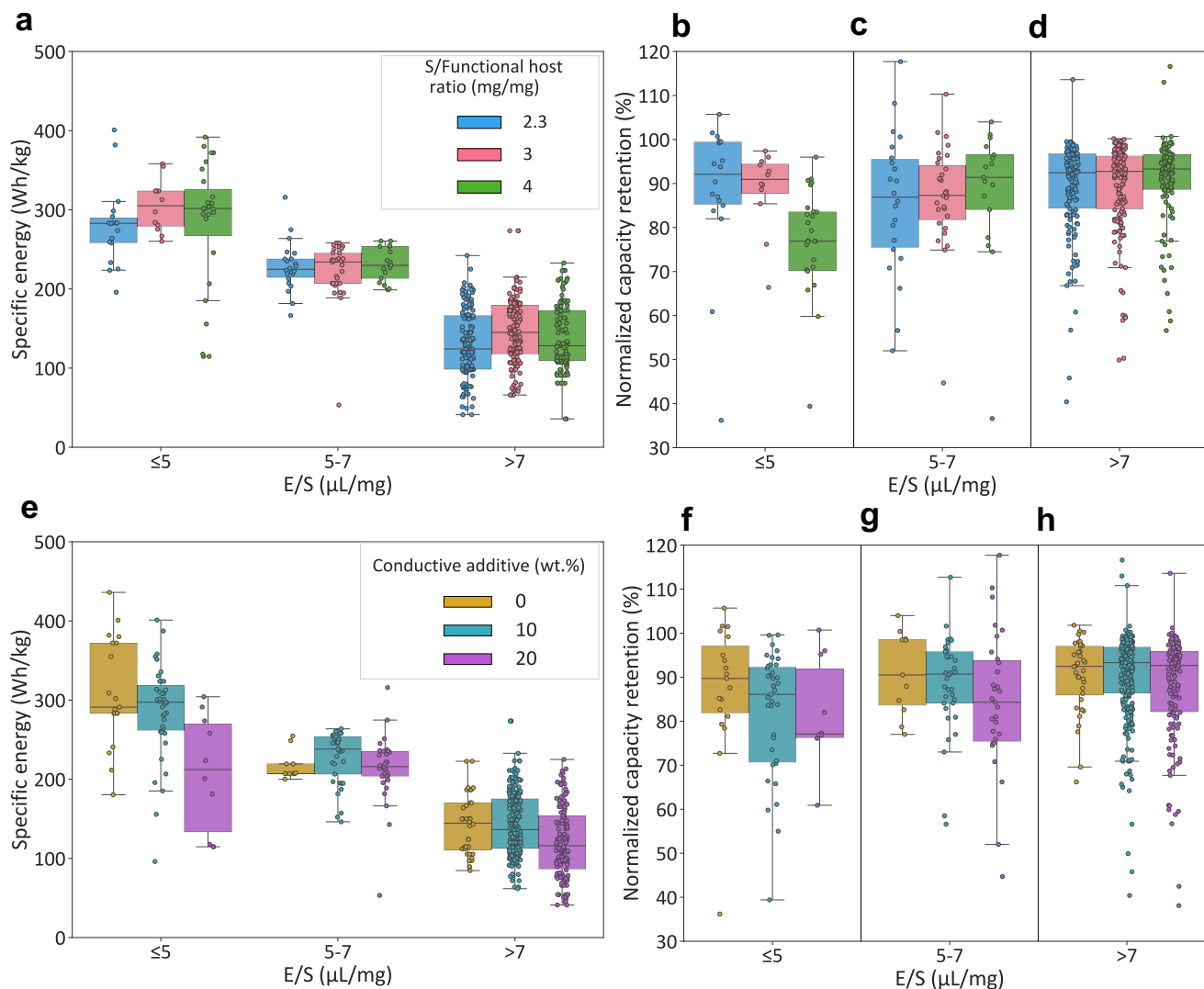
Fig. 4 | Synergistic effects of design parameters under lean electrolyte conditions. The effect of sulfur-to-functional host ratio, and E/S ratio on (**a**) cell specific energy and (**b–d**) cell capacity retention. The effect of conductive additive wt.%, and E/S ratio on (**e**) cell specific energy and (**f–h**) cell capacity retention. We categorized the E/S ratio into three levels: ratios above 7 μl/mg indicate excess electrolyte, 5–7 μl/mg represents below-median but not lean conditions, and below 5 μl/ mg signifies lean electrolyte conditions. Due to limited data, further refinement of the E/S ratio was not feasible. For the conductive additive (wt.%) and the sulfur-to-functional host ratio, we selected the three most representative values based on the data shown in Fig. S3. Refer to Fig. 3b for definition of box elements. Box median and sample size, n, are provided in Table S5. Source data are provided as a Source Data file.

electrochemical impedance spectroscopy (EIS)—each offering a distinct perspective on reaction kinetics.

Exploring synergies in lean electrolyte condition. A close examination of Table 2 reveals that cells with high specific energy typically contain little to no conductive additives, alongside a reduced sulfur-to-functional host ratio. This underscores the importance of investigating potential synergies between these design elements with lean electrolyte conditions. In Fig. 4a, the effect of sulfur-to-functional host ratio on specific energy at different E/S ratios are shown in a series of boxplots. Here we will specifically look at the *median* values for our comparison (Table S5) as it does not skew by extreme values, unlike the mean. Regardless of the sulfur-to-functional host ratio, a reduction in the E/S ratio consistently leads to an increase in specific energy. However, across different E/S ratios, a sulfur-to-functional host ratio of 3 yields cells with slightly higher specific energy. When the ratio is increased to 4, the additional sulfur content can compromise the host's functionality, resulting in a lower discharge capacity. Conversely, with a ratio of 2.3, the lower sulfur content reduces the specific

capacity. Thus, there is an optimal sulfur-to-functional host ratio where specific energy is maximized. While it is an important observation, there is no significant evidence of synergy between E/S and the sulfur-to-functional host ratio regarding specific energy.

The effect of sulfur-to-functional host ratio on capacity retention at different E/S ratios are shown in Fig. 4b–d. Since cells with lean electrolyte conditions typically use thicker electrodes and are cycled at lower C-rates, comparing capacity retention across Fig. 4b–d is less straightforward. The key finding from these figures is that in higher electrolyte volumes (above 5 μL/mg), a higher sulfur-to-functional host ratio improves capacity retention, while in lower electrolyte volumes, a smaller ratio is more effective. When electrolyte is low and sulfur content is high, polysulfide saturation hampers redox reactions, accelerating sulfur loss and reducing capacity. Conversely, in high electrolyte volumes and low sulfur-to-host ratios, excessive catalytic sites, a characteristic feature in functional hosts[67], may lead to undesired side reactions, or enhanced polysulfide dissolution rates, often evidenced by increased rate of self-discharge[68], leading to rapid capacity loss. The optimal sulfur-to-functional host ratio for capacity

retention and energy optimization at low electrolyte volumes is found to be 3, striking a balance between maximizing sulfur utilization and minimizing resistance.

Figure 4e highlights the synergistic effect of conductive additive content and the E/S ratio on specific energy. At high electrolyte volumes, reducing carbon content has little impact on specific energy, but lower carbon levels still slightly favor higher specific energy. At medium electrolyte volumes (5–7 µL/mg), the optimal conductive additive content is 10 wt.%. Under lean electrolyte conditions (≤5 µL/mg), less carbon leads to higher energy density, likely due to increased sulfur content and better utilization. Cells with 0 wt.% carbon show a significant increase in specific energy from 207 Wh/kg to 291 Wh/kg when the E/S ratio drops below 5 µL/mg. In contrast, with 20 wt.% carbon, the energy density remains nearly unchanged. This suggests high carbon content is detrimental under lean conditions, while low carbon content works synergistically with lean electrolyte volumes. Additionally, Fig. 4f–h show that carbon additive has minimal effect on capacity retention at high E/S ratios (>7 µL/mg). In the 5–7 µL/mg range, 10 wt.% carbon is optimal for retention, but with lower E/S ratios, 0 wt.% carbon achieves the highest capacity retention, indicating that smaller electrolyte volumes require less carbon for sustained cycling.

The peculiar sensitivity of the LSB performance to the interplay between lean electrolyte condition and conductive additive can be explained in the context of the effective electronic and ionic transport properties of a sulfur porous electrode. The spatial arrangement of the carbon-binder domain affects ion mobility, influencing ohmic and diffusion overpotentials[69]. The tortuosity (τ) of the porous medium, which measures how complex the transport paths are, plays a key role −higher tortuosity ($\tau > 1$) hinders ion transport, reducing the effective diffusion coefficient (D_{eff}). Vierrath et al.[70] studied the morphology of the carbon-binder domain in a $LiCoO_2$ electrode. They reported a total pore space tortuosity of 1.6–2, with the tortuosity within the carbon-binder domain ranging from 2.5 to 3.5. Mistry et al.[71] observed that increasing the carbon-binder domain from 5 wt.% to 20 wt.% raised the pore network tortuosity from ~6 to 9 in $LiNi_xMn_yCo_{1-x-y}O_2$ electrodes. These findings suggest that in LSBs, where the carbon-binder domain can constitute up to 30 wt.%, their role in determining the charge transport limitations is indispensable. The presence of any spatial heterogeneity such as non-uniform electrolyte wetting, which can possibly exacerbate at high carbon contents, can further impede ionic transport.

The complex relationship between carbon content and the E/S ratio is emphasized in guidelines for developing practical LSBs[65]. Notably, around 50% of the studies in our dataset use 20 wt.% carbon, despite the common recommendation to reduce carbon content for more efficient electrolyte use. While our findings confirm established principles, they also highlight these inconsistencies, offering a data-driven perspective that emphasizes the practical implications and stresses the need to approach these concerns with greater care in research and real-world applications.

LSB rate capability and cyclability at high C-Rates. Figure 5 presents the sensitivity of the LSBs' rate capability to electrode and cell design. The median values are shown in Table S6–S9. The effect of the sulfur-to-functional-host ratio on rate capability (Fig. 5a) is erratic and unpredictable, with discharge capacities being closely competitive. Unlike this, the influence of conductive additive content is significant (Fig. 5b), with lower carbon additive amounts generally and unexpectedly leading to higher discharge capacities across most C-rates. Notably, cells with 10 wt.% carbon outperform those with 20 wt.%, while cells with 0 wt.% carbon show competitive performance at low C-rates but struggle at higher C-rates. As discussed earlier, excessive carbon additives can negatively affect ion transport despite enhancing electronic conductivity. Small amounts is crucial, as carbon additives

maintain long-range electronic conductivity necessary at higher C-rates, but excessive amounts hinder performance. The reliance of LSBs to carbon additives should be reduced by improving electronic conductivity of sulfur hosts (See Table S10).

Figure 5c shows that the highest rate capability in cells is achieved with sulfur loadings up to 2 mg/cm². As sulfur loading rises from 1–2 mg/cm² to 6–8 mg/cm², the median discharge capacity at 0.1 C drops from 1225 mAh/g to 882 mAh/g. This trend of decreasing capacity is consistent across higher C-rates, indicating that thicker electrodes exacerbates transport limitations. Fig. S11c shows the rate of capacity drop as a function of C-rate across different sulfur loading ranges. In the ranges 0–1 and 1–2 mg/cm², an increase in C-rate from 0.1 C to 5 C reduces discharge capacity by about 50%, while at the 4–6 mg/cm² range, the drop is around 60%. In other ranges, the behavior is chaotic or unpredictable due to lack of sufficient datapoints.

Figure 5d illustrates that the E/S ratio significantly influences rate capability, with optimal performance observed at moderate ratios of 15 and 20 µL/mg. Low electrolyte volumes restrict ionic transport and often coincide with high sulfur loading, further reducing discharge capacity. Most experiments focused on E/S ratios of 15 and 20 µL/mg, which proved effective; although higher ratios, such as 25 µL/mg, showed potential for increased capacity. Beyond this value, they typically resulted in a rapid decline in discharge capacity at higher C-rates (Fig. S11d). Excessive electrolyte can exacerbate polysulfide loss and dilute concentrations can negatively impact transport properties. Therefore, proper control of the E/S ratio is essential, as both very low and high values can obscure the true capabilities of the cells unless the study specifically targets lean electrolyte conditions.

To establish a benchmark for the average rate performance of LSBs, we found the median discharge capacity at each C-rate for the cells with sulfur loading of 1.5 mg/cm², a sulfur-to-functional host ratio of 3, a carbon additive percentage of 10 wt.%, and an E/S ratio of 15 µL/mg (i.e., the median values for cell parameters in rate capability experiments). The resulting rated discharge capacities, which serve as performance benchmarks, are as follows: 1191 mAh/g at 0.1 C, 1158 mAh/g at 0.2 C, 1068 mAh/g at 0.5 C, 957 mAh/g at 1 C, 875 mAh/g at 2 C, 762 mAh/g at 3 C, and 634 mAh/g at 5 C. Alternatively, we calculated specific power values (W/kg) and plotted them against specific energy values (Wh/kg) in Ragone plots (Fig. 6a)[72]. Typically, rate capability measurements are conducted with standard cells using high electrolyte content and low sulfur loadings, resulting in most data points clustering below 200 Wh/kg. While LSBs can deliver high power, this is typically observed in lower energy-dense cells, suggesting that energy-dense cells may compromise power performance. Nevertheless, according to our analysis an average LSB cell delivers a discharge capacity of ~0.9 Q_{rev} at 0.1 C, 0.85 Q_{rev} at 0.2 C, 0.69 Q_{rev} at 0.5 C, 0.61 Q_{rev} at 1 C, and 0.57 Q_{rev} at 2 C, respectively. At higher rates of 3 C and 5 C, the confidence intervals are too large to determine reliable Q/Q_{rev} values.

Figure 6a also illustrates the required C-rate for different power output demands, essential for optimizing LSBs for various applications. It highlights approximate power output ranges for high energy density cells, categorized into low (50–150 W/kg, e.g., consumer electronics, grid energy storage, passenger electric vehicles), medium (150–300 W/kg, e.g., electric buses, unmanned aerial vehicles), high (300–500 W/kg, e.g., forklifts, industrial machinery, electric boats), and extreme power demands (above 500 W/kg, e.g., power tools, satellite propulsion systems, and rapid acceleration scenarios). Based on coin-cell measurements, LSBs should discharge at 0.2C–0.5 C for low power applications, around 1 C for medium power needs, 2C–3C for high power, and above 3 C for extreme requirements. Notably, despite their sluggish kinetics, LSBs have made significant strides in handling high discharge rates. However, there is limited data on higher energy density cells, particularly under lean electrolyte and high loading conditions, specifically at the pouch cell level, which hinders
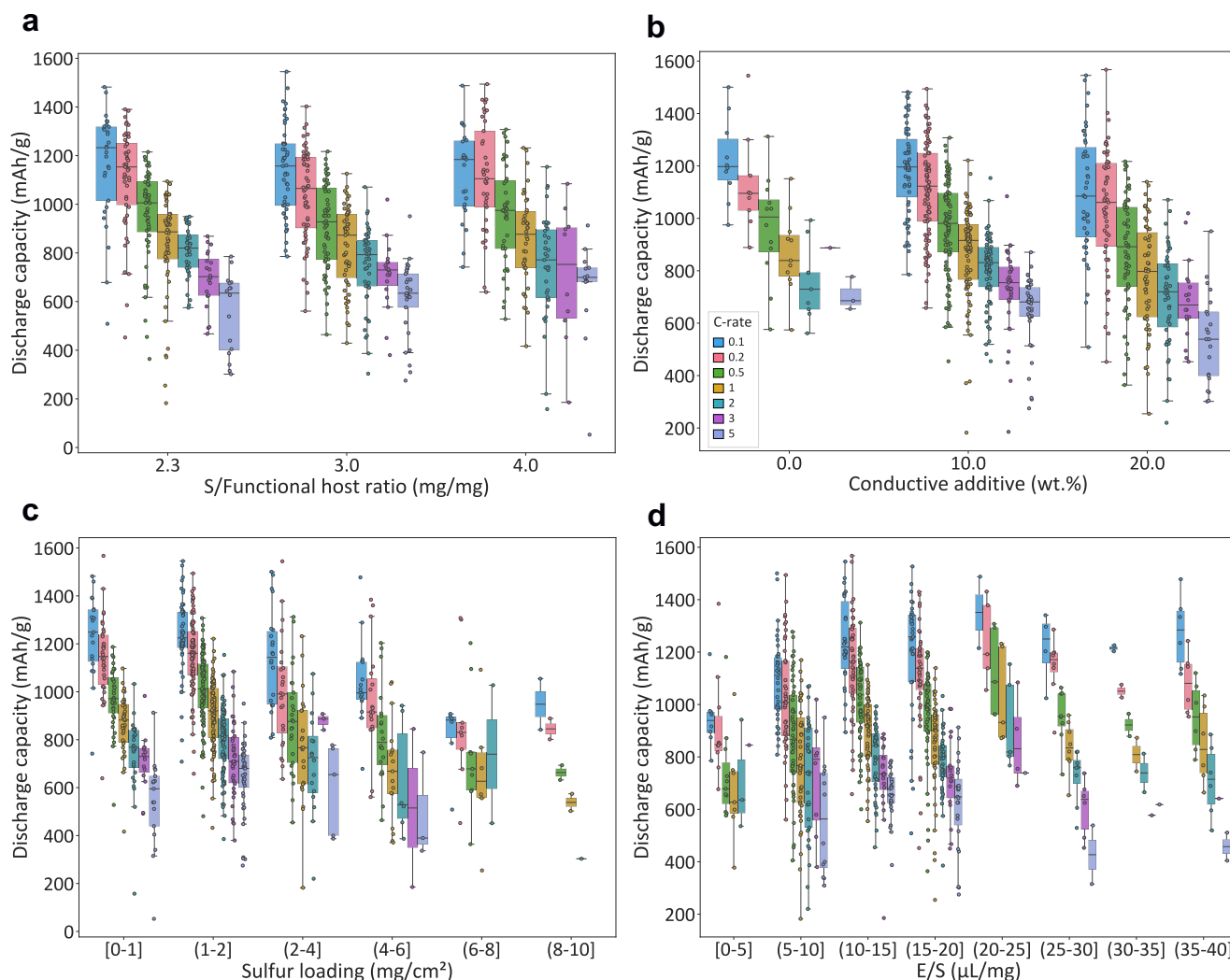
Fig. 5 | Sensitivity of LSB Discharge Rate Capability to Key Electrode and Cell Parameters. The impact of **a** sulfur-to-functional host ratio, **b** conductive additive wt.%, **c** sulfur loading and **d** E/S ratio on LSB cell discharge rate capability. Continuous variables, i.e., sulfur loading and E/S ratio, were categorized into discrete bins for better comparisons across different ranges which might be obscured on a continuous scale. Bins use (i–j] notation: greater than i up to and including j. Typically, at each C-rate the discharge cycle was repeated 3 to 10 times. The values shown for each C-rate represent the average of those repetitions. Refer to Fig. 3b for definition of box elements. Box median and sample size, n, are provided in Table S6–9. Source data are provided as a Source Data file.

accurate performance predictions. This underscores the urgent need for systematic studies to enhance understanding of LSB performance in demanding scenarios.

Figure 6b, presents the rate capability performance of the top 5 percentile of cells having the highest rated discharge capacities[18,73–82]. The median value of the rated discharge capacity for the top 5 percentile was calculated to be 1145 mAh/g at 1 C, 1032 mAh/g at 2 C, 945 mAh/g at 3 C, 944 mAh/g at 4 C, and 871 mAh/g at 5 C, showing a significant improvement compared to those of average cells. These remarkable numbers underscore the role of material improvements in helping LSBs overcome performance barriers (Table S12).

C-rate is an important stress factor for the aging dynamics of the electrochemical systems including LSBs. The sensitivity of the aging to the C-rate is a function of the battery chemistry and its associated degradation mechanisms. For instance, the presence of the degradation phenomena with a large time-constant such as polysulfide shuttle can be underrepresented when the accelerated aging tests are conducted at higher C-rates. Figure 6c shows the capacity retention for different LSB cells cycled at different C-rates normalized to 100-cycles discharge threshold. Initially, it may seem counterintuitive that discharging at higher C-rates results in lower capacity loss. However, this

should be interpreted in view of the coexistence of two different degradation types in LSBs. The first group involves the (electro)chemically-driven side reactions similar to the LIBs. The second group, however, is the transport-driven loss of active material and specific to the LSBs. This second group triggers the direct loss of sulfur through passive flux away from the active sites at the cathode and entails further degradation at the surface of anode, namely the irreversible reactions involving polysulfides, electrolyte, SEI, and Li. At higher C-rates, the electrochemically-driven degradation mechanisms are promoted while the progress of the transport-driven side reactions is limited as the time spent per cycle is shortened. Therefore, we compare the capacity retention of the cells at different C-rates using a discharge-throughput coordinate instead of the cycle number:

$$Q_T^n = \sum_{i=1}^{i=n} Q_i \qquad (5)$$

where Q_T^n is the discharge throughput at cycle number n, which is equal to the cumulative sum of discharge capacities at every cycle, Q_i, from cycle $i = 1$ to $i = n$. According to Fig. 6d we can observe a general trend of decreasing capacity retention with increasing C-rate,
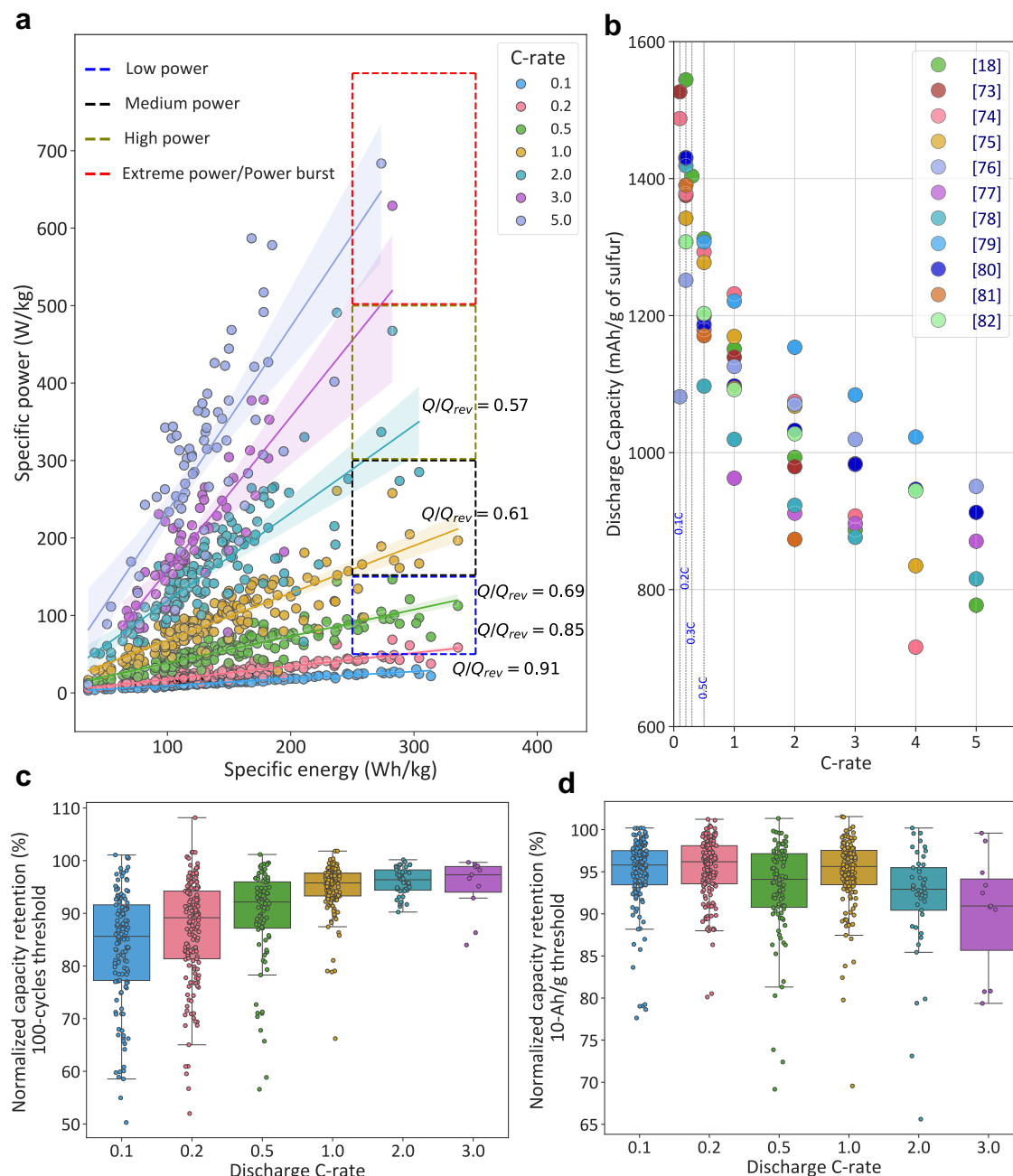
Fig. 6 | LSB Power Performance and High-Rate Cycling Behavior. a Specific power vs. specific energy scatter plot calculated using data from rate capability measurements. Q/Q_{rev} at each C-rate (the slope of the linear regression line, see Eqs. 1 and 2) hints at the average achievable discharge capacity at a given C-rate. **b** top 5% performers of rate capability experiment across all studies. The selection criteria focused on cells that exhibited discharge capacities in the top 5 percentile at 1 C, 2 C, 3 C, 4 C, and 5 C. A cell could excel at just one rate or at several. **c** Effect of discharge C-rate during cycling on capacity retention after certain number of cycles, and **d** after certain amount of discharge throughput. Refer to Fig. 3b for definition of box elements. Box median and sample size, *n*, are provided in Table S11. Source data are provided as a Source Data file.

particularly at 2 C and 3 C (two times faster rate of degradation at 3 C compared to 0.1 C). Overall, Fig. 6c, d show LSBs can technically support higher discharge rates over many cycles, yet this capability results in significant capacity loss over time. This makes current LSBs unsuitable for applications needing stable, frequent high-power cycling. However, LSBs can be advantageous in scenarios prioritizing high energy density with less frequent high-power demands. For these uses, LSBs offer adequate energy density and manage occasional high-power needs effectively. Therefore, matching LSBs to specific applications requires a balance of their cyclability with the power and energy requirements of the intended use.

The faster degradation of LSBs at high discharge rates also stems from issues with the lithium anode, where destabilized SEI layer and uneven lithium plating-stripping increases resistance and the risk of short circuits[83]. To improve LSB lifespan, current density control and stabilized lithium anodes are crucial, especially in designs with thicker sulfur cathodes. Scaling LSBs from coin to pouch cells also introduces significant degradation challenges, primarily due to the uneven migration of dissolved polysulfides, which leads to sulfur agglomeration, anode corrosion, and electrolyte depletion[84–86]. Thick cathodes exacerbate these issues by impeding electrolyte diffusion, creating non-uniform degradation across the cell[87]. However, inconsistent

experimental setups in the literature—like varying sulfur loadings, E/S ratios, and cell assembly details among coin cells and pouch cells (Fig. S12)—make it difficult to evaluate the scalability of LSB materials. A coordinated, standardized approach to pouch cell design and testing is essential for transitioning LSBs to reliable, practical applications.

Outlook

In this study, we compiled data from various sources in the LSB literature that explore the use of sulfur host materials to advance this technology. We aimed to benchmark and standardize the data, and conducting univariate analysis on individual parameters to identify clear and consistent trends. The significant advancements in LSB technology highlight the ongoing dedication of researchers to refine and enhance this innovative battery system.

Achieving a cell specific energy of 500 Wh/kg now seems within reach, as functional sulfur host materials have already enabled cells to demonstrate specific energy levels up to 441 Wh/kg. To optimize LSB fabrication further, several key factors must be addressed. Specifically, sulfur loading and electrolyte-to-sulfur ratio must be carefully optimized to minimize charge transport limitations. Excessive sulfur loading, typically above 6 mg/cm², often results in a decrease in reversible discharge capacity and thus a reduction in specific energy. Future research should explore novel electrode coating methods, such as solvent-free coating, to enable thicker electrodes or refine existing technologies, such as optimizing electrode porosity through calendaring or careful optimization of the size and distribution of active material particles. These adjustments may also reveal potential synergies with lean electrolyte conditions. For instance, our analysis found a constructive synergy in lean electrolyte environments when relatively low amounts of carbon conductive additive were used. This suggests that imbalances in electrode design can significantly influence performance, particularly under lean electrolyte conditions, or alternatively, benefit from synergies that enhance overall efficiency.

Moreover, exploring new electrolyte systems, including sparingly and highly solvating electrolytes, should be prioritized because of their promise for lower electrolyte-to-sulfur ratios. The mechanistic reaction pathways of sulfur are closely tied to electrolyte chemistry, particularly the solvation and solubility of polysulfides, which are crucial for optimizing cycling stability under lean electrolyte conditions. Sparingly solvating electrolytes can restrict polysulfide solubility and facilitate quasi-solid-state reactions, potentially enabling lean electrolyte operation if kinetics can be managed. Conversely, highly solvating electrolytes can promote high polysulfide solubility, ensuring that sufficient lithium polysulfides are available even in lean conditions. Additionally, understanding the interactions between these electrolytes and sulfur hosts could lead to enhanced battery performance and stability.

The design of sulfur host materials hinges on optimizing both structural and functional attribute for effective confinement of polysulfides and Li₂S precipitation. Our analysis reveals that 2D and hollow structures are particularly promising, offering a balanced surface area, and possibly improved electrolyte access, and efficient sulfur impregnation. While surface area is critical, excessively high values can negatively impact performance due to small pores and hindered lithium-ion diffusion. Furthermore, optimal polysulfide adsorption plays a significant role in electrochemical performance, with the most promising results occurring at low to moderate binding energies rather than the highest.

Our analysis of LSB rate capability reveals that their performance is strongly influenced by electrode and cell design parameters. While the sulfur-to-host ratio exhibits unpredictable effects, the content of conductive additives has a significant impact on discharge capacity, with excessive carbon hindering ion transport. To standardize comparisons between different studies, we recommend that sulfur loading be maintained around 1–2 mg/cm², and electrolyte-to-sulfur ratios be

kept within the range of 15–20 µL/mg, as these values are commonly used in most studies. Benchmarking rate performance shows that the top 5 percentile of LSBs achieves a median discharge capacity of 1145 mAh/g at 1 C, 1032 mAh/g at 2 C, 945 mAh/g at 3 C, 944 mAh/g at 4 C, and 871 mAh/g at 5 C, indicating substantial improvements in material innovation. While LSBs can deliver high power, this is typically observed in lower energy-dense cells, with higher energy cells at risk of sacrificing power performance. Although LSBs maintain competitive discharge capacities across various C-rates, their long-term stability at high rates remains a challenge, due to reasons such as lithium anode instability. Furthermore, scaling LSBs from coin to pouch cells introduces challenges which requires standardized testing methodologies and systematic studies for unlocking the full potential of LSBs in real-world applications.

Methods

Literature search and plot extraction
The process of selecting articles for the analysis involved a systematic search across various publisher websites, utilizing specific keywords such as "Li-S" and "Lithium-Sulfur" to pinpoint relevant academic publications. Given the substantial number of scholarly articles available on this topic, a criterion was established to streamline the selection process. Only articles published within a recent five-year window, specifically from 2019 to 2023, were considered. To further manage the volume of data and ensure a comprehensive yet feasible scope of review, a cap of 25 articles per journal was set to stop a data extraction loop. The entire selection methodology, including the criteria and the step-by-step process, is detailed in Fig. S13a, and Table S13. Following the selection of the articles, the next phase focused on extracting quantitative data. Information on electrode formulation, sulfur loading, and electrolyte volume, specific surface area, and polysulfide binding energy was manually extracted from the text of each article, without using automated tools. Numerical data from galvanostatic cycling and rate capability plots (Fig. S13b) were obtained using WebPlotDigitizer (https://automeris.io/), a web-based tool specifically designed to digitize data from graphical representations like plots and graphs. The sources of the articles selected for analysis are provided in the Supplementary Data file.

Statistical methods
Q^s_{rev} values needed to calculate E_s, where extracted from the first cycle discharge capacity of either rate capability plots (starting from 0.1 C) or galvanostatic cycling experiments (discharging at 0.1 C). In experiments where discharge capacity at 0.1 C was unavailable (i.e., cells with different sulfur loading and E/S ratios cycled at a C-rate other than 0.1 C), Q^s_{rev} were estimated using a regression model. Features considered included sulfur loading, E/S ratio, conductive additive wt.%, sulfur wt.%, sulfur-to-functional host ratio, and functional host wt.%. Notably, loading and E/S ratio were expected to strongly affect Q_{rev} and thus were prioritized in the regression analysis. After comprehensive analysis involving multiple features, sulfur loading (M), E/S ratio (γ), and conductive additive wt.% (χ) emerged as the optimal predictors. We have:

$$Q^s_{rev-predicted} = \beta_1 M + \beta_2 \gamma + \beta_3 \chi \qquad (6)$$

where β_1, β_2, and β_3 coefficient where obtained by a multiple linear regress analysis of available Q^s_{rev} data. Subsequently, predicted specific energy values where calculated using Eq. 1. (See Fig. S14).

In our dataset, lifecycle measurements ranged from as few as 50 cycles to over 1000 cycles. Normalized capacity retention was determined by calculating the slope of discharge capacity versus cycle number across the entire range. However, an arbitrary threshold of 100 cycles (or 10 Ah/g) was chosen to enable comparison across different cells. The slope, k, was computed by Theil-Sen estimator which

fits a robust linear regression line by choosing the median slope from all possible pairs of points in a dataset. Unlike simple linear regression, which requires normal distribution of errors, the Theil-Sen estimator is less affected by outliers and relaxes the assumption of normality in error distribution[88]. The Theil-Sen estimator computes the median of slopes between all pairs of points (x_i, y_i) and (x_j, y_j) giving robustness against outliers. The slope k_{TS} of the Theil-Sen estimator is:

$$k_{TS} = median\left(\frac{y_j - y_i}{x_j - x_i}\right) \qquad (7)$$

where the median is taken over all (i,j) pairs with $i < j$. k_{TS} represents the robust estimate of the slope for the linear regression model. A comparison between simple linear regression and the Theil-Sen estimator for plots exhibiting the largest deviations between the two fitting methods is given in Fig. S15. The Theil-Sen estimator provides a more robust fit, particularly in cases where there are significant capacity drops in the initial cycles or when the discharge capacity initially increases with cycling before beginning to decline. The normalized capacity retention, $Q_{retention}$, after an arbitrary p number of cycles is then:

$$Q_{retention} = \frac{Q_1 - (-k_{TS} \times p)}{Q_1} \times 100 \qquad (8)$$

Where Q_1 is the discharge capacity in the first cycle. Here we chose $p = 100$.

The Pearson correlation coefficient, which calculated the strength of linear relationship between two variable of X and Y, in pair plots, was calculated by:

$$r = \frac{\sum (X_i - \bar{X})(Y_i - \bar{Y})}{\sqrt{\sum (X_i - \bar{X})^2 (Y_i - \bar{Y})^2}} \qquad (9)$$

where X_i and Y_i are the individual data points and $\bar{X}$ and $\bar{Y}$ are the means of X and Y values. r values ranges from −1 to 1. A value of 1 indicates a perfect positive linear correlation, while −1 indicates a perfect negative linear correlation.

Data availability
All data that support the findings of this study are available in the Supplementary Data file. Source data are provided with this paper.

References
1. Zhou, G., Chen, H. & Cui, Y. Formulating energy density for designing practical lithium–sulfur batteries. *Nat. Energy* **7**, 312–319 (2022).
2. Bruce, P. G., Freunberger, S. A., Hardwick, L. J. & Tarascon, J. M. Li–O₂ and Li–S batteries with high energy storage. *Nat. Mater.* **11**, 172–172 (2011).
3. Zhang, S. S. Liquid electrolyte lithium/sulfur battery: fundamental chemistry, problems, and solutions. *J. Power Sour.* **231**, 153–162 (2013).
4. Lim, W. G., Kim, S., Jo, C. & Lee, J. A Comprehensive review of materials with catalytic effects in Li–S batteries: enhanced redox kinetics. *Angew. Chem. Int. Ed.* **58**, 18746–18757 (2019).
5. Pang, Q., Liang, X., Kwok, C. Y. & Nazar, L. F. Advances in lithium-sulfur batteries based on multifunctional cathodes and electrolytes. *Nat. Energy* **1**, 16132 (2016).
6. Hong, H., Che Mohamad, N. A. R., Chae, K., Marques Mota, F. & Kim, D. H. The lithium metal anode in Li-S batteries: challenges and recent progress. *J. Mater. Chem. A* **9**, 10012–10038 (2021).
7. Kasnatscheew, J. et al. A Tutorial into practical capacity and mass balancing of lithium ion batteries. *J. Electrochem. Soc.* **164**, A2479–A2486 (2017).
8. Nanda, S. & Manthiram, A. Lithium degradation in lithium-sulfur batteries: insights into inventory depletion and interphasial evolution with cycling. *Energy Environ. Sci.* **13**, 2501–2514 (2020).
9. Zhao, H. et al. A review on anode for lithium-sulfur batteries: Progress and prospects. *Chem. Eng. J.* **347**, 343–365 (2018).
10. Hamed, H. et al. Demystifying charge transport limitations in the porous electrodes of lithium-ion batteries. *Adv. Energy Mater.* **10**, 2002492 (2020).
11. Li, Z. et al. Lithiated metallic molybdenum disulfide nanosheets for high-performance lithium–sulfur batteries. *Nat. Energy* **8**, 84–93 (2023).
12. Zhong, M. et al. A Cost- and energy density-competitive lithium-sulfur battery. *Energy Storage Mater.* **41**, 588–598 (2021).
13. Won-Gwang, L. et al. Cooperative electronic structure modulator of Fe single- atom electrocatalyst for high energy and long cycle Li–S pouch cell. *Adv. Mater.* **35**, 2208999 (2023).
14. Liu, K. et al. Ultrafast strategy to fabricate sulfur cathodes for high-performance lithium-sulfur batteries. *ACS Appl. Mater. Interfaces* **15**, 31478–31490 (2023).
15. Bin, W. et al. Hafnium diboride spherical superstructure born of 5d-metal Hf-MOF-induced p orbital activity of b atom and enhanced kinetics of sulfur cathode reaction. *Adv. Energy Mater.* **13**, 2300590 (2023).
16. Zhang, X. et al. Single zinc atom aggregates: synergetic interaction to boost fast polysulfide conversion in lithium-sulfur batteries. *Adv. Mater.* **35**, 2208470 (2023).
17. Qin, B. et al. A tandem electrocatalyst with dense heterointerfaces enabling the stepwise conversion of polysulfide in lithium-sulfur batteries. *Energy Storage Mater.* **55**, 445–454 (2023).
18. Wang, Z. Y., Wang, H. M., Liu, S., Li, G. R. & Gao, X. P. To promote the catalytic conversion of polysulfides using Ni-B alloy nanoparticles on carbon nanotube microspheres under high sulfur loading and a lean electrolyte. *ACS Appl. Mater. Interfaces* **13**, 20222–20232 (2021).
19. Wang, Q. et al. Highly dispersed conductive and electrocatalytic mediators enabling rapid polysulfides conversion for lithium sulfur batteries. *Chem. Eng. J.* **476**, 146865 (2023).
20. Zhang, Z. et al. Tantalum-based electrocatalyst for polysulfide catalysis and retention for high-performance lithium-sulfur batteries. *Matter* **3**, 920–934 (2020).
21. Zhang, Z. et al. Reasonably introduced ZnIn₂S₄@C to mediate polysulfide redox for long-life lithium-sulfur batteries. *ACS Appl. Mater. Interfaces* **13**, 14169–14180 (2021).
22. Bin, W. et al. Zinc-assisted cobalt ditelluride polyhedra inducing lattice strain to endow efficient adsorption-catalysis for high-energy lithium–sulfur batteries. *Adv. Mater.* **34**, 2204403 (2022).
23. Xue, W. et al. Intercalation-conversion hybrid cathodes enabling Li–S full-cell architectures with jointly superior gravimetric and volumetric energy densities. *Nat. Energy* **4**, 374–382 (2019).
24. Xue, Y. et al. Engineering checkerboard-like heterostructured sulfur electrocatalyst towards high-performance lithium sulfur batteries. *Chem. Eng. J.* **440**, 135990 (2022).
25. Sun, C. et al. High-tap-density sulfur cathodes made beyond 400 °C for lithium-sulfur cells with balanced gravimetric/volumetric energy densities. *ACS Energy Lett.* **8**, 772–779 (2023).
26. Chu, R., Nguyen, T. T., Bai, Y., Kim, N. H. & Lee, J. H. Uniformly controlled treble boundary using enriched adsorption sites and accelerated catalyst cathode for robust lithium–sulfur batteries. *Adv. Energy Mater.* **12**, 2102805 (2022).
27. Wang, R., Tang, W., Tang, M., Wu, Q. & Li, J. ZIF-derived carbon nanoframes as a polysulfide anchor and conversion mediator for high-performance lithium-sulfur cells. *ACS Appl. Mater. Interfaces* **13**, 21544–21555 (2021).

28. Heng, Z. et al. MXene-derived Ti_nO_{2n-1} quantum dots distributed on porous carbon nanosheets for stable and long-life Li–s batteries: enhanced polysulfide mediation via defect engineering. *Adv. Mater.* **33**, 2008447 (2021).

29. Chen, H. et al. Electrode design with integration of high tortuosity and sulfur-philicity for high-performance lithium-sulfur battery. *Matter* **2**, 1605–1620 (2020).

30. Li, Y. et al. Engineering vacancy-defect atomic Ni sites via biowaste valorisation for high-power kinetics in lithium-sulfur batteries. *Energy Storage Mater.* **54**, 553–562 (2023).

31. He, Z. et al. Three-dimensional structural confinement design of conductive metal oxide for efficient sulfur host in Lithium-sulfur batteries. *Chem. Eng. J.* **448**, 137656 (2022).

32. Li, M. et al. Efficient immobilization and bidirectional catalysis of polysulfide conversion by FeCoP quantum dots for lithium-sulfur batteries. *J. Mater. Chem. A* **11**, 11141–11152 (2023).

33. Wang, J. et al. Engineering the conductive network of metal oxide-based sulfur cathode toward efficient and longevous lithium– sulfur batteries. *Adv. Energy Mater.* **10**, 2002076 (2020).

34. Zhou, Z. et al. High-entropy nanoparticle constructed porous honeycomb as a 3D sulfur host for lithium polysulfide adsorption and catalytic conversion in Li-S batteries. *J. Mater. Chem. A* **11**, 5883–5894 (2023).

35. Wang, X. et al. Creating edge sites within the 2D metal-organic framework boosts redox kinetics in lithium–sulfur batteries. *Adv. Energy Mater.* **12**, 2201960 (2022).

36. Dan, L. et al. Design of quasi-MOF nanospheres as a dynamic electrocatalyst toward accelerated sulfur reduction reaction for high-performance lithium–sulfur batteries. *Adv. Mater.* **34**, 2105541 (2022).

37. Zhao, X. et al. Ordered macroporous V-doped ZnO framework impregnated with microporous carbon nanocages as multifunctional sulfur reservoir in lithium-sulfur batteries. *Chem. Eng. J.* **431**, 134242 (2022).

38. Wang, M. et al. Nitrogen-doped $CoSe_2$ as a bifunctional catalyst for high areal capacity and lean electrolyte of Li-S battery. *ACS Energy Lett.* **5**, 3041–3050 (2020).

39. Xiao, Y. et al. Engineering configuration compatibility and electronic structure in axially assembled metal-organic framework nanowires for high-performance lithium sulfur batteries. *ACS Energy Lett.* **8**, 5107–5115 (2023).

40. Shen, Z. et al. Cation-doped ZnS catalysts for polysulfide conversion in lithium–sulfur batteries. *Nat. Catal.* **5**, 555–563 (2022).

41. Tsao, Y. et al. A Nickel-decorated carbon flower/sulfur cathode for lean-electrolyte lithium–sulfur batteries. *Adv. Energy Mater.* **11**, 2101449 (2021).

42. Li, H. J. et al. Quantitatively regulating defects of 2D tungsten selenide to enhance catalytic ability for polysulfide conversion in a lithium sulfur battery. *Energy Storage Mater.* **45**, 1229–1237 (2022).

43. Lei, J. et al. Single-dispersed polyoxometalate clusters embedded on multilayer graphene as a bifunctional electrocatalyst for efficient Li-S batteries. *Nat. Commun.* **13**, 202 (2022).

44. Zou, K. et al. Defect engineering in a multiple confined geometry for robust lithium–sulfur batteries. *Adv. Energy Mater.* **12**, 2103981 (2022).

45. Wei, W. et al. Atomic-level design rules of metal-cation-doped catalysts: manipulating electron affinity/ionic radius of doped cations for accelerating sulfur redox kinetics in Li–S batteries. *Energy Environ. Sci.* **16**, 2669–2683 (2023).

46. Tong, Z. et al. A spatially efficient 'tube-in-tube' hybrid for durable sulfur electrochemistry. *J. Mater. Chem. A* **10**, 5460–5469 (2022).

47. Zhang, X., Liu, Z., Liu, W., Han, J. & Lv, W. Ultrathin carbon-shell-encapsulated cobalt nanoparticles with balanced activity and stability for lithium-sulfur batteries. *ACS Appl. Mater. Interfaces* **15**, 19002–19010 (2023).

48. Zhou, W. et al. One-dimensional confined p-n junction Co_3S_4/MoS_2 interface nanorods significantly enhance polysulfide redox kinetics for Li-S batteries. *J. Mater. Chem. A* **11**, 926–936 (2022).

49. Li, S. et al. Implanting single-atom N_2-Fe-B_2 catalytic sites in carbon hosts to stabilize high-loading and lean-electrolyte lithium-sulfur batteries. *Energy Storage Mater.* **55**, 94–104 (2023).

50. Lu, Y. et al. Dry electrode technology, the rising star in solid-state battery industrialization. *Matter* **5**, 876–898 (2022).

51. Reynolds, C. D., Hare, S. D., Slater, P. R., Simmons, M. J. H. & Kendrick, E. Rheology and structure of lithium-ion battery electrode slurries. *Energy Technol.* **10**, 2200545 (2022).

52. Fan, F. Y. & Chiang, Y.-M. Electrodeposition kinetics in Li-S batteries: effects of low electrolyte/sulfur ratios and deposition surface composition. *J. Electrochem. Soc.* **164**, A917–A922 (2017).

53. Liu, Y. et al. Electrolyte solutions design for lithium-sulfur batteries. *Joule* **5**, 2323–2364 (2021).

54. Gordin, M. L. et al. Bis(2,2,2-trifluoroethyl) ether as an electrolyte co-solvent for mitigating self-discharge in lithium - sulfur batteries. *ACS Appl. Mater. Interfaces* **6**, 8006–8010 (2014).

55. Jing, Z. et al. High-fluorinated electrolytes for Li–S batteries. *Adv. Energy Mater.* **9**, 1803774 (2019).

56. Lee, C. W. et al. Directing the lithium-sulfur reaction pathway via sparingly solvating electrolytes for high energy density batteries. *ACS Cent. Sci.* **3**, 605–613 (2017).

57. Pang, Q. et al. Tuning the electrolyte network structure to invoke quasi-solid state sulfur conversion and suppress lithium dendrite formation in Li–S batteries. *Nat. Energy* **3**, 783–791 (2018).

58. Schneider, H. et al. On the Electrode potentials in lithium-sulfur batteries and their solvent-dependence. *J. Electrochem. Soc.* **161**, A1399–A1406 (2014).

59. Pan, W. et al. Improving the electrochemical performance of Li_2S cathodes based on point defect control with cation/anion dual doping. *J. Mater. Chem. A* **11**, 24637–24643 (2023).

60. Fujita, Y. et al. Lithium sulfite enhances cycle performance of all-solid-state batteries with Li_2S-based positive electrode materials. *ACS Appl. Energy Mater.* **7**, 5447–5456 (2024).

61. Wu, J. et al. Xanthate-mediated oxidation of Li_2S as the lithium-containing cathode in lithium–sulfur batteries with extremely low overpotential. *Adv. Mater.* **36**, 2411525 (2024).

62. Qi, X. et al. Air-Stable Li_2S cathodes enabled by an in situ-formed Li^+ conductor for graphite-Li_2S pouch cells. *Adv. Energy Mater.* **36**, 2310756 (2024).

63. Zhou, L., Danilov, D. L., Eichel, R. A. & Notten, P. H. L. Host materials anchoring polysulfides in Li–S batteries reviewed. *Adv. Energy Mater.* **11**, 2001304 (2021).

64. Klein, M. J., Veith, G. M. & Manthiram, A. Rational design of lithium-sulfur battery cathodes based on experimentally determined maximum active material thickness. *J. Am. Chem. Soc.* **139**, 9229–9237 (2017).

65. Bhargav, A., He, J., Gupta, A. & Manthiram, A. Lithium-sulfur batteries: attaining the critical metrics. *Joule* **4**, 285–291 (2020).

66. Jain, R. et al. Nanostructuring versus microstructuring in battery electrodes. *Nat. Rev. Mater.* **7**, 736–746 (2022).

67. Hart, C. J. et al. Rational design of sulphur host materials for Li-S batteries: correlating lithium polysulphide adsorptivity and self-discharge capacity loss. *Chem. Commun.* **51**, 2308–2311 (2015).

68. Yari, S., Henderick, L., Choobar, B. G., Detavernier, C. & Safari, M. Toward a synergistic optimization of porous electrode formulation and polysulfide regulation in lithium–sulfur batteries. *Small* **20**, 2307090 (2024).

69. Yari, S. et al. Probing charge transport and microstructural attributes in solvent- versus water-based electrodes with a spotlight on Li–S battery cathode. *Adv. Energy Mater.* **14**, 2402163 (2024).

70. Vierrath, S. et al. Morphology of nanoporous carbon-binder domains in Li-ion batteries — A FIB-SEM study. *Electrochem. Commun.* **60**, 176–179 (2015).

71. Mistry, A. et al. Quantifying negative effects of carbon-binder networks from electrochemical performance of porous Li-ion electrodes. *J. Electrochem. Soc.* **168**, 070536 (2021).

72. Beyers, I., Bensmann, A. & Hanke-Rauschenbach, R. Ragone plots revisited: a review of methodology and application across energy storage technologies. *J. Energy Storage* **73**, 109097 (2023).

73. Meng, R. et al. A Tandem electrocatalysis of sulfur reduction by bimetal 2D MOFs. *Adv. Energy Mater.* **11**, 2102819 (2021).

74. Yan, W., Chen, S., Wen, M., Wu, Q. & Yu, S. Multicore closely packed ultrathin-MnO_2@N-doped carbon-gear yolk-shell micro-nanostructures as highly efficient sulfur hosts for Li-S batteries. *J. Mater. Chem. A* **9**, 2276–2283 (2021).

75. Yang, Z. et al. Engineering bimetal phosphorus trisulfides hetero-interface in semi-open frame structure for lithium-sulfur batteries. *Chem. Eng. J.* **475**, 146229 (2023).

76. Liu, J., Xue, M., Zhou, Y., Liu, S. & Yan, T. Effective chemisorption of polysulfides through organic molecules for high-performance lithium–sulfur batteries. *Chem. Eng. J.* **459**, 141556 (2023).

77. Yang, J. et al. Fundamental role of Fe-N-C active sites in a CO_2-derived ultra-porous carbon electrode for inhibiting shuttle phenomena in Li-S batteries. *J. Mater. Chem. A* **9**, 23660–23674 (2021).

78. Dong, C. et al. Boosting bi-directional redox of sulfur with dual metal single atom pairs in carbon spheres toward high-rate and long-cycling lithium–sulfur battery. *Adv. Energy Mater.* **13**, 2301505 (2023).

79. Jung, E. et al. Oxygen-plasma-treated Fe-N-C catalysts with dual binding sites for enhanced electrocatalytic polysulfide conversion in lithium-sulfur batteries. *ACS Energy Lett.* **7**, 2646–2653 (2022).

80. Lin, H. et al. Simultaneous cobalt and phosphorous doping of MoS_2 for improved catalytic performance on polysulfide conversion in lithium–sulfur batteries. *Adv. Energy Mater.* **9**, 1902096 (2019).

81. Zhou, X., Liu, T., Zhao, G., Yang, X. & Guo, H. Cooperative catalytic interface accelerates redox kinetics of sulfur species for high-performance Li-S batteries. *Energy Storage Mater.* **40**, 139–149 (2021).

82. Zhou, Z. et al. A hollow Co0.12Ni1.88S2/NiO heterostructure that synergistically facilitates lithium polysulfide adsorption and conversion for lithium-sulfur batteries. *Energy Storage Mater.* **51**, 486–499 (2022).

83. Chen, K. H. et al. Dead lithium: mass transport effects on voltage, capacity, and failure of lithium metal anodes. *J. Mater. Chem. A* **5**, 11671–11681 (2017).

84. Kong, L. et al. Nonuniform Redistribution of sulfur and lithium upon cycling: probing the origin of capacity fading in lithium–sulfur pouch cells. *Energy Technol.* **7**, 1900111 (2019).

85. Das, S. et al. Optimization of the form factors of advanced Li-S pouch cells. *Small* **20**, 2311850 (2024).

86. Chen, Z.-X. et al. Failure analysis of high-energy-density lithium–sulfur pouch cells. *Energy Storage Mater.* **53**, 315–321 (2022).

87. Shi, L. et al. Reaction heterogeneity in practical high-energy lithium-sulfur pouch cells. *Energy Environ. Sci.* **13**, 3620–3632 (2020).

88. Ohlson, J. A. & Kim, S. Linear valuation without OLS: the Theil-Sen estimation approach. *Rev. Account. Stud.* **20**, 395–435 (2015).

Acknowledgements

Author contributions

S.Y. and A.C.R. conceived the study, performed data extraction, quantitative analysis, and wrote the original draft. Q.P. conceived the study, contributed to data interpretation, and reviewed and edited the manuscript. M.S. conceived the study, contributed to data interpretation, reviewed and edited the manuscript, and supervised the research.

Competing interests

The authors declare no competing interests.

Additional information

Supplementary information The online version contains supplementary material available at https://doi.org/10.1038/s41467-025-60528-4.

Correspondence and requests for materials should be addressed to Mohammadhosein Safari.

Peer review information Nature Communications thanks Gaoran Li and the other, anonymous, reviewer(s) for their contribution to the peer review of this work. [A peer review file is available].

Reprints and permissions information is available at http://www.nature.com/reprints

Publisher's note Springer Nature remains neutral with regard to jurisdictional claims in published maps and institutional affiliations.